JOM
https://doi.org/10.1007/s11837-021-05071-5

What Can Plastic Flow Fields Tell Us About Heat Sources in Deformation Processing?

ANIRUDH UDUPA ,[1,6] NARAYAN K SUNDARAM,[2] ANIRBAN MAHATO,[3] TATSUYA SUGIHARA,[4] JAMES B MANN,[5] and SRINIVASAN CHANDRASEKAR[1]

1.—Center for Materials Processing and Tribology, Purdue University, West Lafayette, IN, USA. 2.—Department of Civil Engineering, Indian Institute of Science, Bangalore, India. 3.—Department of Mechanical Engineering, Indian Institute of Technology, Patna, India. 4.—Department of Mechanical Engineering, Osaka University, Osaka, Japan. 5.—M4 Sciences, Lafayette, IN, USA. 6.—e-mail: audupa@purdue.edu

We characterize primary (shape-change) and secondary (friction) deformation, and associated temperature fields, in metal cutting and forming processes, using in situ imaging and simulation. The experimental configurations enable access to the deformation zones and die contact interfaces, for measuring deformation, temperature, and frictional drag. Infrared thermography reveals that the plastic strain-rate field is an excellent proxy for the deformation-induced heat sources. Both spatially confined and diffuse strain-rate fields occur, depending on the initial workpiece deformation state. When the strain rate is confined, as in prehardened material, the temperature modeling is greatly simplified, as the heat source is also now localized. However complex, microstructure-driven deformation modes, such as sinuous flow in annealed metals, result in spatially diffuse strain-rate and body heat sources that are more challenging to analyze. Our unified measurements should be of value for accurately estimating the fraction of plastic dissipation that is converted into heat in large-strain deformation processes.

INTRODUCTION

Manufacturing processes for metals such as machining, forming, and sliding-based processing involve large-strain plastic deformation and friction at die–workpiece contacts.[1–3] The frictional interaction at die–tool contacts during processing, in contrast to conventional sliding friction, is usually also coupled to large-strain deformation occurring in a very thin wall layer adjoining the contact interface. This coupling is a consequence of the severe contact conditions including high pressure and shear stresses, elevated temperatures, and intimate contact.[2,4–7] The friction-induced deformation is usually referred to as secondary deformation, as it is not directly involved in the primary shape change. It is however a major contributor to redundant deformation in processing (non-shape change deformation) and influences the microstructure and mechanical properties of the workpiece surface, both directly and, indirectly, via the temperature field.[1,3] Since most of the work of plastic deformation is converted into heat,[8,9] the deformation fields in the primary and secondary zones determine workpiece and die/tool temperatures, microstructure, and property changes, and die wear. This connection between deformation and heating in processing was recognized even 150 years ago by Tresca, in observations of heat lines in forging.[10] Any modeling, prediction, and control of temperature and thermal effects thus necessarily requires understanding of the plastic flow fields, and their quantitative characterization.

In this study, we examine the characteristics of the primary (shape-change) and secondary (friction) deformation, and associated temperature fields, in machining and deformation processing of metals using in situ imaging, complemented by finite

(Received September 17, 2021; accepted November 22, 2021)

Published online: 13 January 2022

element (FE) simulation. The imaging is carried out in the visible and infrared (IR) wavelength regimes. We obtain a quantitative description of the deformation-induced heat source intensities and spatial extent, with a view to analyzing temperature fields. Using diverse examples from cutting, sliding, and forming, we show the occurrence of both uniform and nonuniform plastic flow. While the strains involved are quite large, what determines the temperature field is the rate of heat generation; this is fixed by the strain-rate field rather than the strain field. When the strain rate is concentrated, the temperature modeling is simplified irrespective of whether the deformation is uniform or not because of the localization of the heat source. The challenge in temperature modeling is however significant when the strain-rate field is diffuse or dispersed. The concentration, or lack thereof, of the strain rate is strongly influenced by the initial material deformation state, including grain-level anisotropy of the flow stress. We also examine, at high resolution, the attributes of the deformation layer adjoining the die wall, the temperature field therein, and the coupling between die–workpiece friction and localized plasticity in the contact. Experimental configurations, for accessing different regions of the workpiece deformation zone and "often-hidden" tool–die contact interfaces, to enable temperature, displacement, and frictional drag measurements, are highlighted. The paper closes with specific conclusions about analysis of temperature fields in processing and some of the challenges ahead.

EXPERIMENTAL PROCEDURES

The large-strain plastic flow fields illustrative of various deformation processes are studied experimentally using model two-dimensional (2D) deformation (plane-strain) configurations representative of machining, incremental forming, and piercing/punching. The model configurations are (1) cutting with a hard wedge (tool), (2) sliding of a hard wedge (die), and (3) wedge indentation. The deformation and temperature fields are characterized, quantitatively, using in situ imaging of metal flow coupled with digital image correlation (DIC) analysis, and in situ IR thermography. The objective is to understand the intensity and spatial distribution of heat sources that determine the temperature fields.

Figure 1 illustrates the imaging using 2D cutting/sliding as the deformation process. (Note that, for the case of punching/piercing, the sliding setup is replaced by a wedge indentation system.) A metal plate workpiece is moved against a (fixed) hard steel wedge (die/tool) at speeds V_o of up to 10 mm/s under conditions of plane strain. The workpiece comprises one of the following alloys: commercially pure Al, oxygen-free high thermal conductivity (OFHC) copper, and CP-Ti in plate form, with different initial deformation states (e.g., annealed, half-hard). For the present study, the specific alloy system is less important because the results pertaining to the deformation and temperature fields are quite typical. A polished glass block is clamped against the workpiece to constrain side flow of material (2D deformation) and facilitate imaging. The experiments are carried out on a linear slide instrumented to measure the two principal force components: in the sliding direction (power component) and the normal loading force. The forces also enable the process energy to be estimated and correlated with energy estimates made from the mesoscale deformation measurements. A smaller set of high-speed cutting experiments (75 m/min to 220 m/min) was carried out using rotary 2D turning of brass and Al tubular workpieces; this configuration is discussed below.

The flow of material in the process zone is imaged in situ, from a side of the workpiece and through the glass block, using a high-speed camera (PCO dimax; Photron WX-100) coupled to an optical microscope assembly (Nikon Optiphot) (Fig. 1). The camera could record at up to $\sim$ 5000 fps with sensor areas as large as 1296 $\times$ 720 pixels. A 5$\times$, 10$\times$, or 20$\times$ objective lens is used with the microscope, with a maximum field of view of 4.3 mm $\times$ 2.4 mm and a highest spatial resolution of $\sim$ 1 μm/pixel. The highest-resolution configuration is particularly useful for characterizing flow in the immediate vicinity of the tool face, which reflects the friction condition. The image sequences are analyzed using DIC, to estimate deformation parameters, viz. effective (von Mises) strain rate and effective strain.[11,12] Pathlines and streaklines are also constructed from the flow fields.[12] The strain-rate and strain measurements also enable the process energy distribution in various regions of the workpiece, including the die–workpiece contact, to be mapped. The image correlation and deformation computation are implemented using a custom MATLAB program; details are provided in Appendix 1.

The temperature field in cutting is measured using in situ infrared (IR) imaging at both low and high speeds. This is done with (1) a viewing configuration analogous to Fig. 1 for the primary deformation zone temperature and (2) an optically and IR transparent sapphire tool, to access the tool–chip contact along the rake face, for the secondary deformation zone temperature. The measurements enable correlation of the temperature with deformation field attributes. Appendix 2 describes the temperature measurements in detail and the experimental configurations.

Wedge indenters with rake angle α of –70° to +15° are used as the tools and dies, covering the spectrum of sliding and cutting (Fig. 1). The experimental parameters are defined in the figure. The sliding experiments mimic local deformation in processes such as incremental forming,[13] extrusion and drawing,[1,3] and friction stir processing. The punching experiment, wherein the plastic flow in the wall

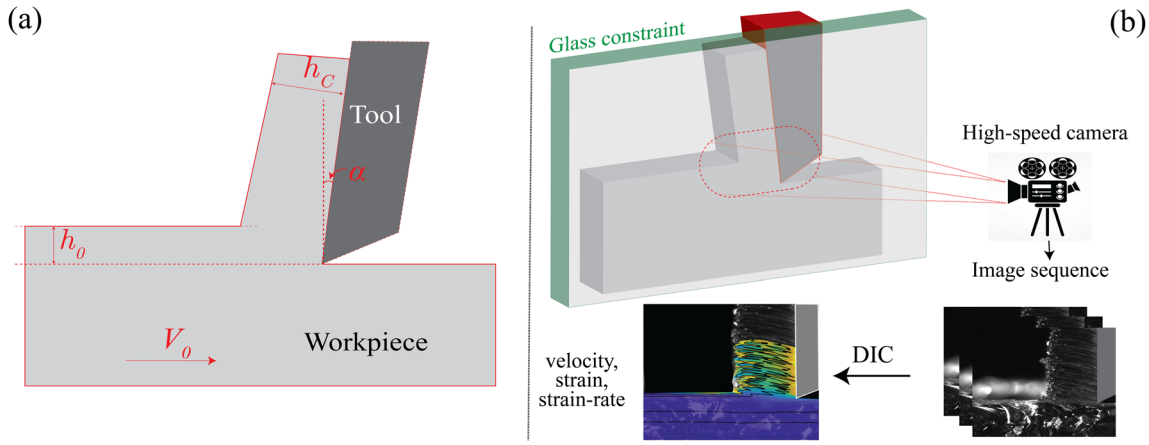

Fig. 1. Plane-strain deformation configuration for in situ observations of material flow. (a) Schematic of 2D cutting process. Tool rake angle is α, and undeformed chip thickness is h_0. (b) High-speed imaging of material flow and analysis of deformation.

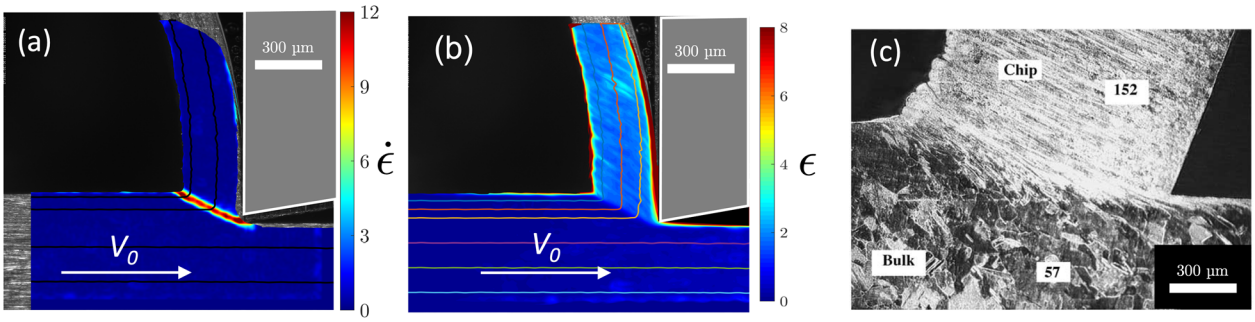

Fig. 2. Cutting of prestrained Cu (prestrain $\sim$ 2) shows laminar flow with highly localized strain rate (shear plane). (a) Strain-rate field and streaklines superimposed onto one frame from a high-speed image sequence showing confined deformation zone. (b) Strain map showing uniform straining with smooth streaklines (laminar flow). (c) Microstructure of partially formed OFHC copper chip showing narrow deformation zone and "flow-line"-type chip microstructure indicative of large-strain deformation. Also shown are average Vickers hardness values (kg/mm^2) measured in the workpiece bulk and chip.

layers adjoining the die–workpiece contact is mapped, is done with a wedge with apex angle of 30°. This configuration, which mimics processes such as piercing and deep drawing, is found to be well suited for studying deformation layers adjoining die walls, which arise from frictional drag. All experiments are done dry unless otherwise stated. The experiments are complemented by FE simulations of polycrystalline aggregate sliding (Al-1100) and cutting (OFHC copper); the simulation procedures are described in detail in Refs. 14 and 15 respectively.

RESULTS

We present the measured deformation and temperature fields from the various processes and use these examples to highlight the close coupling between strain rate, heat generation, and temperature. The strain-rate field attributes are used to motivate a discussion of prediction of temperature fields in deformation processing.

Machining Deformation and Temperature Fields

Figure 2a shows one frame from a high-speed image sequence of chip formation in cutting of prestrained (strain $\sim$ 2) copper. The background color shows the strain-rate field at steady state, which represents the deformation zone. It is evident that the chip forms by a process of intense shear that is confined to a narrow zone ($\sim$ 30 μm thickness), which can be idealized as a shear plane. While the steady-state strain rate is highly spatially localized, the strain field that is developed in the chip is uniform with smooth streaklines of flow (Fig. 2b). This uniform deformation is reflected in the measured strain value being constant at $\sim$ 2.5 throughout the chip. We refer to this type of flow as laminar, using an analogy from fluid dynamics. Such imaging observations, dating back even to the 1940s using cinematography as well as observations of deformation of grids inscribed in the workpiece, have largely confirmed the so-called shear plane

model of chip formation.[2] The strain rate in the confined deformation zone in Fig. 2a is ~ 10/s; this is quite large given that the cutting speed is only 3 mm/s. Since the strain rate varies approximately linearly with cutting speed, the measurements show that, at practical cutting speeds of 2 m/s to 3 m/s, the strain rates will be very large, ~ 10^4/s. The intense shear-plane deformation causes a sharp transition in the microstructure as illustrated in Fig. 2c, which shows a quick stop micrograph of the deformation region in cutting of Cu. The equiaxed ~ 100-μm grains in the sample bulk are transformed into flowlines by the localized shearing over a very narrow zone. The flow lines comprise thin (submicrometer) elongated grains, too small to be resolved by the optical microscopy.

Note that a localization of the strain rate in a deformation process does not automatically fix the nature of the strain field (uniform, localized, etc.). In certain instances, e.g., involving shear banding, both the strain and strain rate are highly localized, concurrently, whereas in laminar-flow chip formation (Fig. 2), only the strain rate is localized while the strain is uniform.

The close correspondence between the high-strain-rate region and the temperature field is illustrated in Fig. 3, taken from cutting of CP-Ti. The figure shows both the primary deformation region (left) via the DIC strain-rate field, and the temperature distribution obtained via IR thermography (right). Based on the strain rate, the primary deformation region comprises two distinct zones: a fan-shaped deformation zone well ahead of the tool wherein the strain rate is relatively small but increasing gradually, followed by a narrow zone of localized severe deformation, just ahead of the tool, in which the strain rate is much higher. The representative strain rate in the zone of localized deformation is ~ 40/s, for this relatively low machining speed of 10 mm/s. The effective strain imposed in the peeled chip is ~ 1.5 as estimated by DIC. Two distinct zones of temperature are also seen in the temperature field (Fig. 3, right), paralleling the strain-rate field. The fan-shaped, small-strain-rate zone is characterized by a temperature of 80°C to 100°C with relatively gentle temperature gradients, while a representative temperature of ~ 140°C, with much steeper gradients, is characteristic of the zone of localized severe deformation. The highest temperature of ~ 160°C occurs in a region of the chip that partially overlaps with the severe deformation zone. The latter is a consequence of an additional temperature rise due to a friction-induced heat source adjoining the tool face. The "wall layer" and the friction-induced deformation in this contact region are discussed below. No shear banding (strain localization) was observed in this experiment. This type of close correspondence between the strain-rate and temperature fields has also been observed in cutting experiments on various Al and brass alloys. Importantly, the observation reinforces the physically consistent description of heat sources in large-strain deformation processes as originating in the strain-rate field.[1,2,5]

Effect of Initial Workpiece Deformation State on Deformation and Heat Sources

The nature of the deformation field is fundamentally different when the initial state of the workpiece is an annealed condition. Figure 4a (experimental) and b (FE simulation) show the strain-rate field, with streaklines superimposed, in cutting of OFHC copper. The streaklines in Fig. 4a show that the deformation is highly unsteady, characterized by large-amplitude folding and significant components of rotation in the flow, a form of unsteady flow called sinuous flow.[16] The chip is now essentially composed of a series of large-amplitude folds that are stacked on top of one another. Details of the development of sinuous flow, and its microscale origins in plastic buckling of surface layers ahead of the chip, can be found elsewhere.[12,16] The background color in the figure shows the strain rate, which is quite diffuse, indicative of a deformation zone that is broadly spread out and ill defined. The

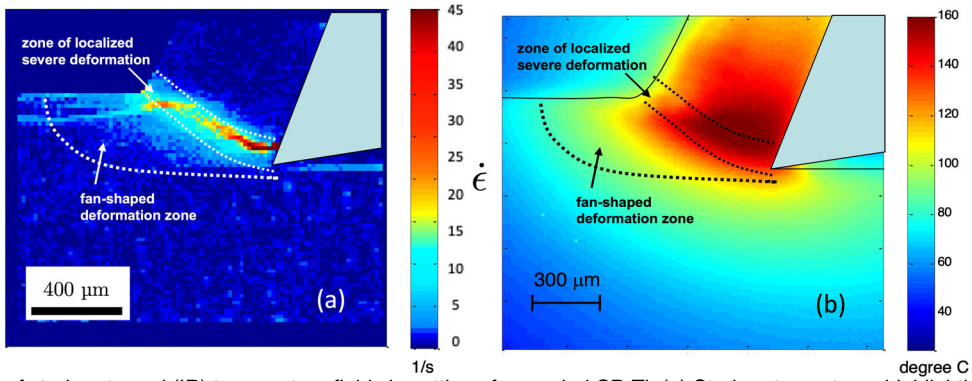

Fig. 3. Comparison of strain-rate and (IR) temperature fields in cutting of annealed CP-Ti. (a) Strain-rate contours highlighting characteristics of the primary deformation region of chip formation. (b) Distribution of temperature in workpiece and chip. Note the strong similarity between the temperature and strain-rate fields.

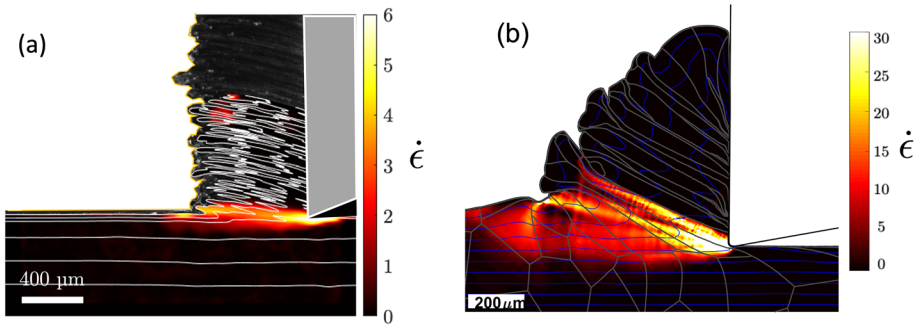

Fig. 4. Low-speed cutting of annealed OFHC Cu results in sinuous flow, characterized by thick-chip, wavy streaklines, material folding, and diffuse deformation zone. (a) One frame from a high-speed in situ image sequence, with strain-rate and streaklines superimposed (V_0 = 0.5 mm/s). (b) Finite-element simulation of cutting of annealed polycrystalline Cu reproduces the sinuous flow, with material folding and diffuse deformation zone (V_0 = 5 mm/s). Note that the deformation zone here is quite spread out, as against the highly confined zone in cutting of prestrained Cu.

unsteady sinuous flow with folding, and diffuse strain-rate field, are also well captured in the finite element (FE) simulation shown in Fig. 4b. The spatially diffuse strain-rate field, and its fluctuation with time (not shown), means that the underlying heat generation (heat sources) is also quite spread out and fluctuating. The challenges in modeling these heat sources are obvious. The unsteady deformation with annealed Cu may be contrasted with the highly localized shear-plane deformation observed in cutting of prestrained OFHC Cu (Fig. 2-a), wherein the heat sources are spatially highly confined and nonfluctuating with time. It is these latter attributes that have enabled analysis of machining temperatures using analytical and computational models.[2,17,18] In fact, the aforementioned difficulty of modeling the temperature field with annealed metals applies equally well also to deformation modeling; to reproduce the unsteady sinuous flow and its characteristics, the FE simulations had to incorporate Voronoi partitioning of the surface into "pseudograins," and model the grain-level inhomogeneity of the flow stress induced by anisotropy and intergrain kinematic constraints.[14,19] Importantly, the results point to the key role of prior workpiece deformation state in determining heat sources in machining-based processing.

The above-discussed influence of the initial workpiece deformation state on the process strain-rate/strain fields is not just a characteristic of cutting; it is seen in practically every type of deformation processing operation. Figures 5a and b shows the strain rate developed in sliding-based deformation processing (5 mm/s), for two different initial workpiece states: prestrained ($\sim$ 1.1) and annealed (strain free), respectively. In Fig. 5a, the strain-rate field delineates three zones of intense deformation (strain rate $\sim$ 6/s), labeled as AO, BO, and CO. These high-strain-rate zones correspond to the zones of intense heat generation. It is this type of strain-rate field, with a pile-up region ahead of the wedge (Fig. 5a), that is usually assumed in slip-line field (SLF) modeling of the sliding deformation process to estimate forces and pressures. In contrast to Fig. 5a, the strain-rate field that develops in the initially annealed workpiece is quite diffuse (Fig. 5-b). Furthermore, the flow is now unsteady (see the streaklines) and characterized by significant rotation components (sinuous flow). It is impossible to reproduce this type of unsteady sinuous flow, with folding, using classical SLF modeling. However, as in the cutting, the sinuous flow pattern is well captured using FE analysis (Fig. 5c) if grain-level variation in flow stress is incorporated into the modeling scheme via, for example, a pseudograin model.[14] The FE analysis also shows the strain-rate field in this case to be diffuse. Furthermore, the strain-rate field was found to fluctuate significantly with time. As with the cutting, the diffuse nature of the strain-rate field (annealed workpiece) poses significant challenges to modeling the heat generation, be it analytically or with FE analysis. In contrast, the heat sources due to the highly localized strain rate (prestrained workpiece) can be well modeled because of their confined nature.

The sliding deformation field also illustrates another divergence between the strain-rate and strain fields noted above in the cutting: the localized strain-rate field in Fig. 5a results in uniform straining of the workpiece in the wake of the wedge (strain $\sim$ 2.5, see figure), whereas the diffuse strain-rate field (Fig. 5b and c) results in inhomogeneous deformation in the workpiece.

Temperature Rise Due to Frictional Heating and Related Contact Condition

The temperature rise due to frictional heating is well illustrated by measurements of the temperature in the tool/die wall region, and its coupling to friction contact conditions therein. We use 2D cutting by turning thin-walled brass 332 (1.7 Wt.% Pb) tubes with 50 mm outer diameter and 1.65 mm wall thickness for this illustration. A sapphire tool, suitably faceted to enable direct observation of the otherwise "hidden" tool–chip interface (Fig. 6a;

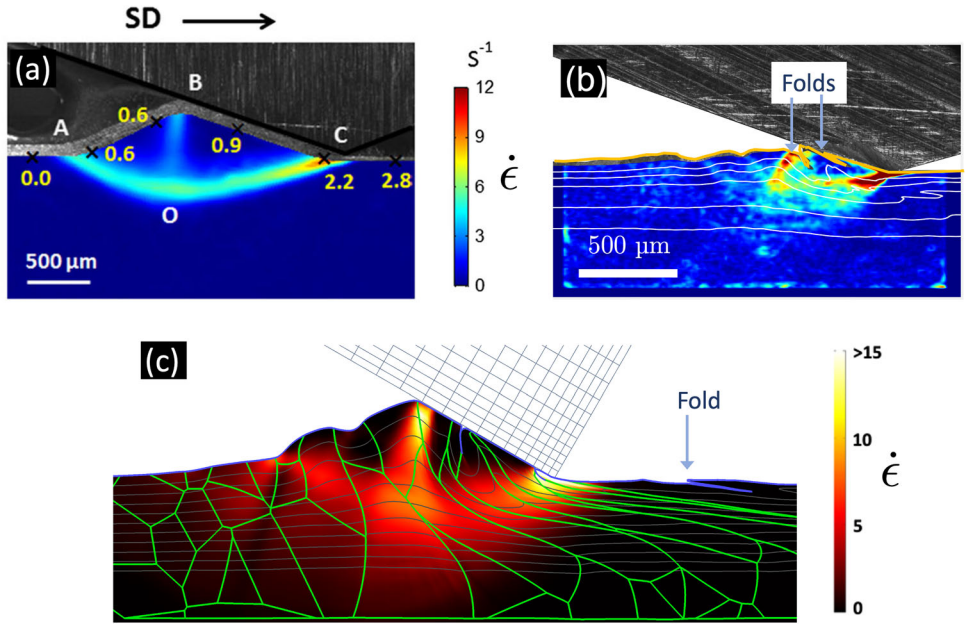

Fig. 5. Sliding of wedge against prestrained and annealed materials, showing important distinctions in strain-rate field. (a) One frame from image sequence of sliding of prestrained Al showing smooth laminar flow with localized strain rate (deformation). The flow results in three distinct, confined deformation (shear) zones. (b) One frame from sliding of annealed Cu showing sinuous flow, material folding, and highly diffuse and unsteady strain-rate field. (c) FE simulation of sliding of an annealed Al pseudograin polycrystal showing diffuse strain-rate field material folding.

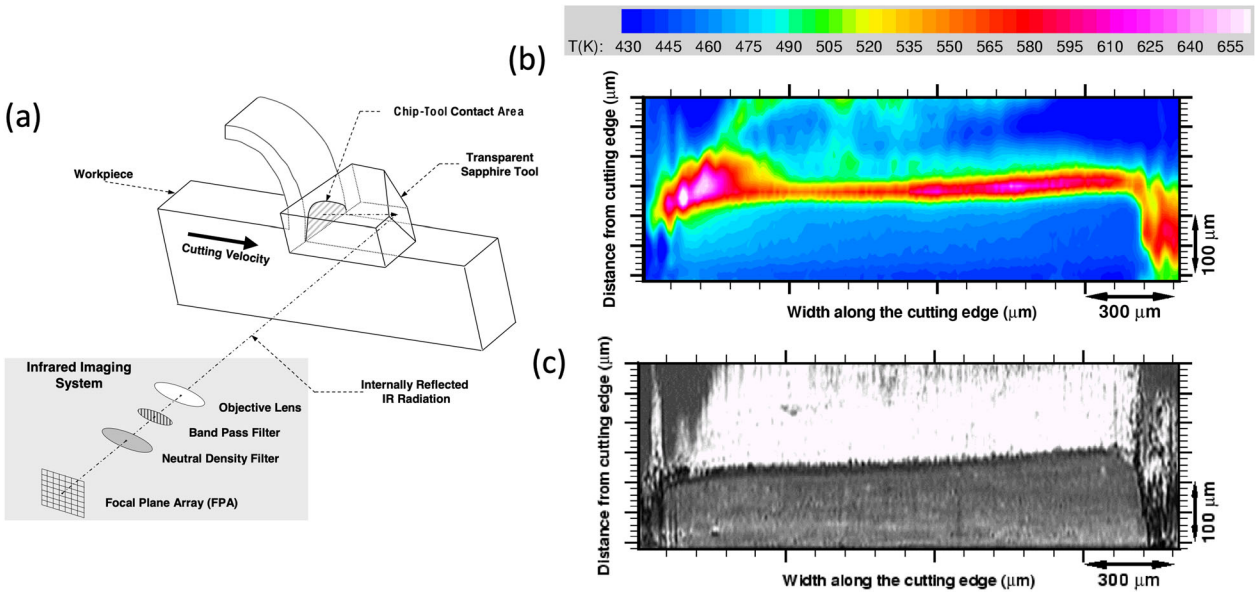

Fig. 6. In situ observations of tool–chip contact region along rake face in high-speed cutting of brass 332 with sapphire tool. (a) Schematic of experimental setup with optically transparent sapphire tool, suitably faceted, to observe the tool–chip contact using total internal reflection. (b) Temperature distribution along contact interface derived from IR imaging. (c) Optical high-speed image of the contact at visible wavelength.

Appendix 2) at both visible and IR wavelengths, is used for the cutting. Details of the imaging are given in Appendix 2. The brass tube is mounted onto the spindle of a machining center and fed against the stationary sapphire tool. The cutting conditions were feed rate of 50 μm/rev or 100 μm/rev, depth of cut of 1.65 mm (tube wall thickness), and (high) speeds in the range of 75 m/min to 220 m/min.

Figures 6b and c show, respectively, the rake face (tool–chip contact) IR temperature field at steady state (V_0 = 90 m/min) and a corresponding optical microscope image of the rake face obtained via high-speed imaging at visible wavelength. The view in these images is analogous to that obtained by "sitting" inside the tool and watching the chip slide across the rake face. The bottom edge in the

temperature field plot, as well as in the optical microscope image, represents the cutting edge. Both images are scaled to the same size for direct comparison. The temperature is relatively constant, ~ 460 K (187°C), along the rake face in a zone extending from the cutting edge up and until about 130 μm from this edge (Fig. 6b). This zone corresponds to one of intimate sliding contact between the chip and tool, albeit with the sliding retarded due to frictional drag, as was inferred from the high-speed imaging. Note that this intimate contact region is characterized by very high normal pressure and shear stresses, typical of die–tool contact regions in deformation processes.[1,2,7] The optical microscope image (Fig. 6c) shows that the intimate contact region (dark) is relatively clear with only lightly scattered specks of metal deposit, indicating negligible metal transfer onto the tool face in this region. Adjoining this intimate contact (drag) region is a (shiny) zone of intermittent, nonintimate contact characterized by conventional sliding. The normal and shear stresses in this latter region are typically much smaller than in the zone of intimate contact.[5,20] There is, however, significant metal transfer herein, which gives the region its shiny appearance in the image (Fig. 6c). The relatively narrow transition region separating the intimate contact and conventional sliding regions is marked by streaky metal deposits. The highest contact temperature of ~ 625 K (352°C) is seen to occur in this transition region, well away from the cutting edge (Fig. 6b). Similar zones of high temperature occur along the lateral (or transverse) sides of the chip–tool contact (see, for example, at the arrow in this figure, concomitant with gross metal transfer). The temperature in the conventional sliding region, extending beyond the high-temperature zone, is also roughly constant, with approximately the same temperature value as in the intimate contact region.

Replicate experiments carried out using the same machining condition showed good reproducibility of both the temperature field and contact conditions (e.g., drag, metal transfer). The highest temperature in the contact was in the range of 625 K to 690 K (352°C to 417°C) in the replicate experiments. The metal transfer region was found to become became smaller in extent with increasing speed.

Frictional Drag at Die and Tool Walls

To understand the frictional drag and associated deformation-induced temperature rise, such as the results presented in Fig. 6, it is useful to examine the material flow in the immediate vicinity of die and tool surfaces. While this may be done for specific cutting and forming configurations, a more general examination of these frictional–deformation attributes can be done using quasistatic (wedge) indentation (Fig. 7, inset). The normal and shear stresses at a wedge–indentation contact, as in hardness testing, are quite large, replicating the severe contact conditions typical of forming and machining interfaces.[6] The frictional drag can be further amplified, for the purpose of study, by using narrow-angle wedge indenters (apex angle < 60°). Hence, we examined material flow and deformation field in plane-strain wedge indentation of Al 1100 (annealed, 23HV) using a 30° apex-angle wedge at speed of 0.1 mm/s (quasistatic). The indentation was done dry as well as with a lubricant. The material flow in the very vicinity of the wedge (die) wall was mapped using high-speed imaging (PCO dimax CMOS camera) and the imaging configuration of Fig. 1. The displacement, strain-rate, and strain fields in the immediate vicinity of the wall were obtained by DIC analysis.

Figure 7a and b shows the retardation of material flow near the indenter wall due to friction based on tracking of two sets of (digital) marker points embedded very close to the indenter wall. Also shown in the figures is the distortion of virtual grid lines (yellow), that were initially straight and oriented perpendicular to the indenter face. In Fig. 7a, corresponding to the beginning of the indentation, the two sets of marker points, one set in the indenter and the other in the material, are identically located. At a later stage of the indentation, the two sets are displaced relative to one another (Fig. 7b). Likewise, the initially straight grid lines are seen to be stretched parallel to the indenter face, and curved, highlighting the frictional drag. By tracking several such sets of markers and grid lines, we could obtain quantitative and qualitative characterizations of the displacement field in the indenter–workpiece contact region, and of the strain (Fig. 7c) and strain-rate fields, at various stages of the indentation. Several observations about the interconnection between friction and material flow can be made from the figure. Firstly, the frictional drag is evident from the displacement field (Fig. 7b). Also, the distance from the wall to which the friction influence extends is well demarcated (wall drag layer). Secondly, there is slip at the indenter–workpiece interface with the narrow-angle indenter. Whether slip occurs at a die wall has been a long-standing question in deformation processing and machining, and this is a key boundary condition in computational simulations of deformation and die-wall temperatures. It may be of interest to note here that, in fluid mechanics, the no-slip wall boundary condition for viscous fluid flow was an important discovery.[21] Wall slip may however be less likely to occur with wide-angle indenters, because of the compression mode of deformation prevailing in the volume under the indenter. Thirdly, the strain field is highly localized, extending only ~ 10 μm away from the contact interface; the strain in this region is also quite large, ~ 5 (Fig. 7c). It is this intense deformation in the wall region, with associated high strain rate, that results in large friction energy dissipation and associated temperature rise, such as in Fig. 6b. Many of these

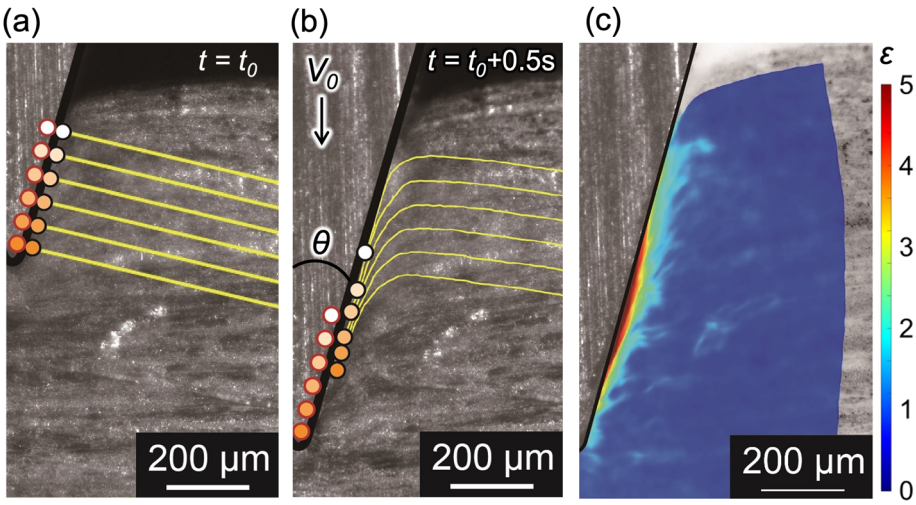

Fig. 7. High-speed in situ imaging of quasistatic wedge indentation of annealed Al to characterize frictional drag at indenter wall. (a) Virtual grid lines and grid points just prior to loading. (b) Displacement of grid lines and points after indenter loading, highlighting material flow and frictional drag. Note the wall slip. (c) Strain field in wall contact region.

observations related to wall drag have also been well reproduced in FE simulations.[22] This type of mapping of the deformation field in the wall region should be of value for accurate modeling (and model validation) of the temperature rise due to friction in forming and machining processes. Fourthly, the wall deformation likely contributes the major component of the actual friction, unlike in conventional engineering sliding contacts.

Similar flow-mapping observations showed that, when a lubricant was applied to the contact, (a) the extent of the wall slip increased, and (b) the thickness of the wall-drag layer adjoining the contact interface was significantly reduced. Interestingly, this change (reduction) in drag was also reflected in the indentation force, which decreased by 30%. Together, the observations indicate that the frictional drag and associated dissipation are greatly reduced if a fluid is active in the contact zone. This should result in smaller contact-zone temperatures during processing.

The high-resolution displacement measurements enabled a material model to be fit to the wall deformation layer. The material flow in the wall layer was found to resemble that of a Bingham fluid with dynamic viscosity of ~ 12 mPa s. Further study of the wall layer characteristics, currently ongoing, should provide insights into other questions such as whether this layer resembles a classical fluid mechanical boundary layer, confirmation of wall slip and the effect of lubricant, and quantification of the friction-induced heating and energy dissipation in this layer. The observations also suggest that narrow-angle indentation provides a good general framework for studying die wall friction layers of relevance for deformation processing.

Implications for Temperature Analysis

The study has shown, using model examples from cutting, sliding, and punching (indentation), the diverse nature and attributes of the large-strain, plastic deformation field and related temperature field that prevail in deformation processes. Both the primary deformation, which determines shape change, and the secondary deformation related to frictional drag have been characterized quantitatively as well as phenomenologically. The strain-rate field, which determines the rate of heat generation (via the integrated product of strain rate and flow stress) is strongly correlated with the temperature field (see, e.g., Fig. 3). While the frictional drag at the die wall is tightly coupled to the deformation field in the immediate vicinity of this contact (Fig. 7) and determines the local contact-temperature field therein via an additional deformation-induced, heat-source contribution (Fig. 6). The initial workpiece deformation state is found to play a key role in determining the attributes of the strain-rate and strain fields, and the nature of the plastic flow evolution (Figs. 2, 4 and 5). Experimental configurations for carrying out in situ observations of the workpiece primary deformation zone and tool/die wall region frictional drag have also been described (Figs. 1, 6; Appendix 2). These configurations offer a general framework for measuring processing temperatures and material flow, concurrently, in model systems that mimic deformation processes.

The results offer some insights into modeling of temperature fields in large-strain deformation processing and the challenges thereof. We may consider the temperature field in any general deformation process to be a superposition of the temperature rises due to the primary deformation and friction-related secondary deformation.[2] Considering first

the primary-deformation-related temperature rise, the key characteristic that determines the heat source and rate of heat generation is the strain-rate field. With prestrained workpieces, in plane-strain deformation, the strain-rate fields are seen to be highly localized (Figs. 2a and 5a). These will give rise to highly localized, moving "planar" heat sources, very typical of processing operations.[23] A similar situation prevails with shear bands in processing; here, too, the underlying heat source (strain rate) is highly localized and the resulting deformation (strain) is highly unsteady.[24] Modeling of such localized moving heat sources is less challenging and can be treated, in principle, analytically by combining the classical Jaeger analysis[25] of temperature rise due to a moving point/planar source (Green's function) and Blok's pioneering analysis[26] of partition of heat (energy) at interfaces between sliding bodies. The latter is very much needed for deformation processing since, unlike say welding or laser heating, a key feature of heat generation in deformation processing is that it arises from frictional sliding at contact interfaces (e.g., die–workpiece). The partitioning problem can be generalized also to treat additional bodies in the contact vicinity, such as lubricant and chip/wear particle; see, e.g., Refs. 27 and 28. In fact, this type of modeling has been successfully carried out for processes such as sliding, cutting, forming, and grinding.[2,27,29,30] Where necessary, the analytical modeling can be supplemented by computational simulation to address secondary factors such as workpiece geometric complexity and temperature-dependent material properties.

The temperature modeling challenge is much more acute when the strain-rate field is diffuse and unsteady, as in sliding and cutting of metals in an initially annealed state (Figs. 4 and 5b, c). The dispersed strain-rate field then give rises to a heat source that is also distributed diffusely over a finite, relatively large, deformation volume, viz. a body source. Treating this problem is of course significantly more challenging, be it analytically or even numerically, because accurately capturing drivers of diffuse and unsteady strain-rate fields such as sinuous flow (Figs. 4b and 5c) requires modeling the specimen as a polycrystalline aggregate.[14,19] Such a requirement appears to have been overlooked to date in cutting and sliding processing, where the norm has been to treat the workpiece implicitly as being in a prestrained state.

Regarding the die-wall temperature field, our frictional drag observations suggest that this temperature field will be strongly influenced by the nature of this drag and its coupling to the secondary deformation. It is worth pointing out here that the friction force value itself will be determined to a large extent by the details of the secondary deformation field (strain, strain gradient). This is because the secondary-zone plastic deformation is embedded in the ensemble friction force value. It is this coupling to the plastic deformation that makes the nature of friction in various large-strain deformation processes fundamentally different than in engineering systems (e.g., bearings, piston–cylinder) and difficult to model. The observations suggest a path forward via careful quantitative measurement of the wall friction characteristics (e.g., wall-slip, strain-field parameters) in a highly local region ($\sim$ 10 μm) of the die–workpiece contact.

It is perhaps appropriate to conclude with a quantitative examination of the linkage between the energy dissipation at the mesoscale (primary deformation, friction induced, etc.) and ensemble force/energy measurements. This is done in Fig. 8 using the example of cutting of annealed Al. Figure 8a shows the strain-rate field obtained by DIC analysis of material flow. By tracking and integrating along material path lines, the product of the (local) flow stress and strain rate, we can estimate the plastic deformation energy dissipated in the chip and in the workpiece surface/subsurface.[16]

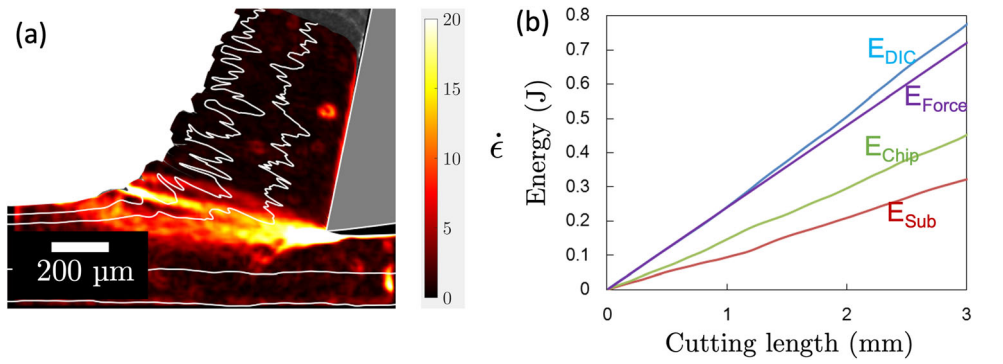

Fig. 8. Energy dissipation in cutting of annealed Al. (a) Strain-rate contours superimposed onto an image frame from a high-speed sequence. By integrating the flow stress along path lines in the strain-rate field, the energy dissipated (E_{DIC}) in the chip and workpiece can be estimated via a bottom-up calculation as $E_{DIC} = E_{Chip} + E_{Sub}$, where E_{chip} and E_{sub} are the energies dissipated in the chip and the subsurface, respectively. (b) Comparison of cutting energy derived from force (E_{force}) measurement (top-down estimation) and the DIC (E_{DIC}). Johnson–Cook parameters used in the bottom-up energy estimation are A = 49 MPa, B = 157 MPa, and n = 0.167.[31]

These energy contributions are plotted as E_{Chip} and E_{Sub}, respectively, in Fig. 8b. A Johnson–Cook material model for annealed Al is assumed (see figure caption for details). The sum of these, E_{DIC}, gives the overall cutting energy as derived from the mesoscale deformation analysis (bottom-up estimate). Another estimate of this energy is obtained from force measurements by taking the product of the cutting force and the length of cutting, a top-down calculation; this is shown as E_{force} in Fig. 8b. The correspondence between the two energy estimates is striking, with the maximum difference being $< 10\%$, even for this highly unsteady sinuous flow case. We have observed similar close agreement for the case of sliding deformation also. This exercise also suggests a way of obtaining an ensemble value for the friction force/energy from wall drag measurements.

CONCLUSION

This study examined the characteristics of the primary (shape-change) and secondary (friction) deformation zones, and associated temperature fields, in model cutting and forming processes using in situ imaging and finite element simulation. Experimental configurations, for accessing the workpiece deformation zone and "often-hidden" tool–die contact interfaces, to enable temperature, displacement, and frictional drag measurements, at the mesoscale are highlighted. The combined measurements and modeling enabled quantitative description of the strain-rate fields, and frictional drag at die walls. These parameters determine the deformation-induced heat source intensities and their spatial extent. The temperature rise due to the primary strain-rate field and frictional drag is measured using infrared thermography and correlated with deformation field parameters, for illustrative example cases. Our examples have also shown diverse types of strain rate and strain fields, e.g., localized or diffuse, arising from the nature of the initial deformation state of the workpiece. Regarding modeling of the temperature field, we show that, when the strain rate is concentrated, the temperature modeling can be greatly simplified, irrespective of whether the deformation (strain) is uniform or not, because of the localization of the heat source. However, this modeling challenge can be significant when the strain-rate field is diffuse or dispersed, due to the occurrence of body heat sources and the need to include material microstructure aspects in the deformation analysis. Concomitant measurements of strain rate, die-wall frictional drag, and temperature at the mesoscale, such as those presented here, should be of value also for accurately estimating what fraction of the (plastic) deformation-induced dissipation is converted into heat in large-strain deformation, which is a quantity of significant relevance to manufacturing processes but for which only limited data exist.

ACKNOWLEDGEMENTS

This research was supported in part by US DOE EERE award DE-EE000786, NSF Grant CMMI 2100568, and US Army Research Office DURIP Award W911NF-17-1-0201 to Purdue University.

CONFLICT OF INTEREST

On behalf of all authors, the corresponding author states that there are no conflicts of interest.

APPENDIX 1: DIC ANALYSIS OF DEFORMATION STRAIN

The DIC algorithm used for deformation analysis consists of the following steps:

i) Pick two consecutive image frames F1 and F2 from an image sequence and divide each of the frames into subimages with resolution of 16×16 pixels.
ii) Compare the subimages from F1 with those of F2 with the cross-correlation function and obtain an estimate of the horizontal and vertical displacements in each subimage.
iii) Collate the estimated displacements for each of the subimages to obtain a displacement field between the two frames.
iv) Use the displacement field to calculate the incremental strain field. We compute and report the von Mises effective strain (scalar) as being representative of this incremental strain.
v) Repeat the process with the subsequent images in the sequence. By accumulating the incremental von Mises strain in each step, the total strain field is obtained.

APPENDIX 2: TEMPERATURE MEASUREMENT BY INFRARED THERMOGRAPHY

This appendix gives details of the configurations used in the study to measure temperatures in various deformation regions, including in the very vicinity of die/tool walls. Equally importantly, the second, sapphire-tool-based experimental approach discussed can also be used to access workpiece and die regions in various deformation processing operations for a variety of process attribute measurements, including interface velocity/drag, temperature, tool and die wear, and lubricant film thickness.[5,20,32]

PRIMARY DEFORMATION ZONE TEMPERATURE FROM SIDE OF THE WORKPIECE

The temperature distribution in the primary deformation zone in low-speed cutting of CP-Ti was measured using an infrared (IR) imaging system, with an imaging configuration very similar to that shown in Fig. 1. For the measurement, one side of the Ti workpiece sample was coated with a "black" paint of high emissivity (ε ~0.92). A medium-wavelength, high-speed IR imaging system (Galileo, Amber-Raytheon) was used to measure the radiation emitted from the deformation region (Fig. 1), using observations from a side of the workpiece. For these measurements, the side of the workpiece was not constrained by the glass block. The imaging system consisted of a charge-coupled device (CCD) detector array and an IR microscope assembly. The microscope assembly focused the radiation onto a two-dimensional focal-plane array (FPA) of 256 × 256 InSb detectors. With the 3× objective lens used in the present study, the size of each of the pixels was 10 μm × 10 μm and the field of view was 2.56 mm × 2.56 mm. The FPA had a time constant low enough to enable system operation at shutter speeds as short as 2 μs, allowing the observation of transient events. A band-pass filter, fit into the microscope assembly, cut off radiation outside a specific spectral range depending on the temperature range of interest. Radiation intensity values were converted to temperature values using a calibration experiment, wherein the IR imaging system was focused onto a heated Ti sample, coated with the same black paint as the cutting sample. The calibration Ti sample was heated using a hot plate. Concurrent with the recording of the radiation intensities, a K-type thermocouple attached to the calibration sample recorded the temperature values. The calibration experiment was done in the temperature range of 30°C to 250°C, the range relevant for the present cutting.

SECONDARY DEFORMATION ZONE TEMPERATURE USING OPTICALLY TRANSPARENT SAPPHIRE TOOL

Figure 6a shows a schematic of the optical arrangement used to observe the chip–tool contact along the rake face at high cutting speeds of 75 m/min to 220 m/min. For this IR radiation measurement, a tube-turning configuration was used, with brass 332 as the workpiece (see also the main section of the paper). A transparent sapphire tool in the form of a parallelepiped, and suitably faceted to allow for internal reflection of the contact interface through a side facet of the tool, was used for the cutting and observations (see figure). Sapphire is transparent to infrared (IR) radiation at wavelengths of 2 μm to 5.3 μm, in addition to having a high index of refraction (> 1.6), and low optical dispersion in this spectral region.

The intensity of IR radiation emitted by the chip–tool interface was collected and measured by an imaging system comprising an IR camera and associated microscope assembly. The system was focused onto the chip–tool interface through the sapphire tool using the aforementioned total internal reflection (Fig. 6a). The IR camera was a medium-wavelength, high-speed, charge-coupled device (CCD)-based thermal imaging system (Galileo made by Amber-Raytheon). The objective lenses for the microscope assembly were made of semiconductor materials, viz. silicon (Si) and germanium (Ge). The lenses focused the radiation onto a 2D focal plane array (FPA) of 256 × 256 detector elements (pixels), effectively creating an image of the source on the FPA. The detector elements were made of indium antimonide (InSb), which is highly sensitive to radiation in the medium-wavelength IR range, allowing temperature changes as small as 0.025°C to be detected in a black body. The FPA had a time constant short enough to enable system operation at shutter speeds as low as 2 μs, allowing for observation of transient events. The microscope assembly was equipped with a rotatable filter wheel onto which two band-pass filters, with spectral ranges of 3.16 μm to 3.80 μm and 4.31 μm to 4.95 μm, were fit. The imaging system could be operated at framing rates of up to 1500 frames per second by sacrificing either the field of view or the spatial resolution. In the present experiments, an integration time of 1.0 ms and frame rate of 100 frames per second were used. By combining radiation intensity measurements made in the two wavelength windows and using the grey-body approximation,[33–35] the temperature field in the tool–chip contact (die-wall) region was obtained. This type of two-color pyrometry has been successfully used to measure temperatures in surface grinding,[36] forming,[33,37,38] and high-speed machining.[34]

REFERENCES

1. W.A. Backofen, *Metall. Trans.* 4, 2679 (1973).
2. M.C. Shaw, *Metal Cutting Principles* (MIT Press, Cambridge, 1957), pp 25–35.
3. W. Johnson and P.B. Mellor, *Engineering Plasticity* (Ellis Horwood, Chichester, 1983), pp 497–514.
4. E.G. Orowan, *Proc. - Inst. Mech. Eng.* 150, 140 (1943).
5. K. Nakayama, *Bull. Fac. Engg. Yokohama Nat. Univ.* 7, 1 (1958).
6. F.P. Bowden and D. Tabor, *Friction: An Introduction to Tribology* (Garden City, Anchor, 1973), pp 95–108.
7. W.R. Wilson and S. Sheu, *Int. J. Mech. Sci.* 30, 475 (1988).
8. W.S. Farren and G.I. Taylor, *Proc. R. Soc. A.* 107, 422 (1925).
9. G.I. Taylor and H. Quinney, *Proc. R. Soc. A.* 143, 307 (1934).
10. M.H. Tresca, *Proc. Inst. Mech. Eng.* 29, 301 (1878).
11. J. Westerweel, E. Gerrit and R.J. Adrian, *Annu. Rev. Fluid Mech.* 45, 409 (2013).
12. A. Udupa, K. Viswanathan, Y. Ho and S. Chandrasekar, *Proc. R. Soc. A.* 473, 20160863 (2017).

13. K. Jackson and J. Allwood, *J. Mater. Process. Technol.* 209, 1158 (2009).
14. A. Udupa, A.S. Vandana, M. Saei, D. Gupta, J.B. Mann, K. Viswanathan and N.K. Sundaram, *Int. J. Mach. Tool Manuf.* 168, 103728 (2021).
15. A.S. Vandana and N.K. Sundaram, *J. Manuf. Processes.* 54, 1 (2020).
16. H. Yeung, K. Viswanathan, W.D. Compton and S. Chandrasekar, *Proc. Natl. Acad. Sci. USA* 112, 9828 (2015).
17. G. Boothroyd, *Proc. Inst. Mech. Eng.* 177, 789 (1963).
18. T.D. Marusich and M. Ortiz, *Int. J Numer. Meth. Eng.* 38, 3675 (1995).
19. N.K. Sundaram, A. Mahato, Y. Guo, K. Viswanathan and S. Chandrasekar, *Acta Mater.* 140, 67 (2017).
20. E.D. Doyle, J.G. Horne and D. Tabor, *Proc. R. Soc. A.* 366, 173 (1979).
21. A.H. Shapiro, *Shape and Flow: The Fluid Dynamics of Drag* (Garden City, Anchor, 1961), pp 109–121.
22. N.K. Sundaram, *Phil. Mag.* 99, 2883 (2019).
23. D. Rosenthal, *Trans. ASME* 68, 849 (1946).
24. D. Sagapuram, K. Viswanathan, A. Mahato, N.K. Sundaram, R. M'Saoubi, K.P. Trumble and S. Chandrasekar, *Proc. R. Soc. A.* 472, 20160167 (2016).
25. J.C. Jaeger, *J. Proc. R. Soc. N. S. W.* 76, 203 (1942).
26. H. Blok, *Proc. Inst. Mech. Eng.* 2, 222 (1937).
27. Y. Ju, T.N. Farris and S. Chandrasekar, *J. Tribol.* 120, 789 (1998).
28. H.S Dhami, P. R. Panda. D. P. Mohanty, A. Udupa, J.B. Mann, K. Viswanathan and S. Chandrasekar, Unified Analysis of Temperature Fields Arising from Large Strain Deformation and Friction in Manufacturing Processes, in TMS 2021 150th Annual Meeting & Exhibition Supplemental Proceedings 2021 (pp. 921–931). Springer, Cham.
29. X. Tian and F.E. Kennedy Jr., *J. Tribol.* 116, 167 (1994).
30. S. Malkin, *J. Eng. Ind.* 96, 1184 (1974).
31. G. Shayegan, H. Mahmoudi, R. Ghelichi, J. Villafuerte, J. Wang, M. Guagliano and H. Jahed, *Mater. Des.* 60, 72 (2014).
32. V. Madhavan, S. Chandrasekar and T.N. Farris, *J. Tribol.* 124, 617 (2002).
33. D.P. DeWitt, G.D. Nutter, ed., *Theory and Practice of Radiation Thermometry* (Wiley, New York, 1988), pp 72–75.
34. A. Hijazi, S. Sachidanandan, R. Singh and V. Madhavan, *Meas. Sci. Technol.* 22, 025106 (2011).
35. P.R. Childs, J.R. Greenwood and C.A. Long, *Rev. Sci. Instrum.* 71, 2959 (2000).
36. J. Hwang, S. Kompella, S. Chandrasekar and T.N. Farris, *J. Tribol.* 125, 377 (2003).
37. M. Failie, W. Fraser, B. Farahbaksh, R. Lamb and O. Meijer, On-Line Temperature Measurement in Hot Rolling of Aluminum Using Infrared Imaging Systems, in Thermosense XI: Intl Conf on Thermal Infrared Sensing for Diagnostics and Control 1989 (Vol. 1094, pp 84–92).
38. B.K. Tsai, D.P. DeWitt and G.J. Dail, *Measurement* 11, 211 (1993).